The Role of the Working Fluid and Nonideal Thermodynamic Effects on Performance of Gas-Lubricated Bearings

De Waart, Wessel; Pini, Matteo

DOI
10.1115/1.4066822

Publication date
2025

Document Version
Final published version

Published in
Journal of Engineering for Gas Turbines and Power

ASME Journal of Engineering for Gas Turbines and Power
Online journal at:
https://asmedigitalcollection.asme.org/gasturbinespower

The Role of the Working Fluid and Nonideal Thermodynamic Effects on Performance of Gas-Lubricated Bearings

Wessel de Waart
Propulsion and Power,
Faculty of Aerospace Engineering,
Delft University of Technology,
Delft 2629 HS, The Netherlands
e-mail: W.deWaart@tudelft.nl

Matteo Pini[1]
Propulsion and Power,
Faculty of Aerospace Engineering,
Delft University of Technology,
Delft 2629 HS, The Netherlands
e-mail: M.Pini@tudelft.nl

Small-scale turbomachinery operating at high rotational speed is a key technology for increasing the power density of energy and propulsion systems. A notable example is the turbine of an organic Rankine cycle turbogenerator for thermal recuperation from prime engines and industrial processes. Such systems typically operate with organic compounds characterized by complex molecular structures to allow the design of efficient fluid machinery and flexibility in matching the heat source and sink temperature profiles. Gas-lubricated bearings are considered advantageous compared to traditional oil-lubricated rolling element bearings for supporting the turbine rotor, enabling greater machine compactness and reduced complexity, and avoiding contamination of the working fluid. In certain operating conditions, however, the lubricant of the gas bearing is in thermodynamic states near the saturated vapor line or in the vicinity of the fluid critical point, whereby nonideal effects are relevant and may affect bearing performance. This work investigates the physics of thin film flows in gas bearings operating with fluids made by complex molecules. The influence of nonideal thermodynamic effects on gas bearing performance is discussed by analysis of the fluid bulk modulus. Reduced values of the nondimensional bulk modulus near the critical point or saturated vapor line decrease bearing performance. The main parameter characterizing the influence of molecular complexity on bearing performance is shown to be the acentric factor. For complex fluids with large acentric factors, the impact of nonideal thermodynamic effects on nondimensional bearing load capacity and rotordynamic characteristics is less pronounced. [DOI: 10.1115/1.4066822]

Keywords: gas bearings, nonideal thermodynamic effects, high-speed turbomachinery

1 Introduction

Small-scale turbomachinery operating at high rotational speeds is an enabling technology for the high-power density propulsion and power systems of the future [1]. Machines with tip diameters on the order of 30 mm and rotor speeds up to 200 krpm have been considered for a variety of applications [2]. Examples of such applications include small turbochargers [3], cryogenic coolers using an inverse Brayton cycle [4], fuel cell air management systems [5], and microgas turbines. More recently, high-speed centrifugal compressors have been investigated for both domestic [6] and airborne [7] heat pump applications, whereas radial-inflow turbines are considered for high-power density thermal energy conversion systems based on the supercritical CO_2 Brayton cycle [8] or the organic Rankine cycle [1].

The requirements of compactness and high efficiency dictate the adoption of gas bearings in high-speed turbomachinery. This type of bearings can support high-speed rotors with low maintenance and at reduced friction loss [9]. Furthermore, the use of the process fluid as a lubricant in the gas bearing allows the elimination of the oil lubrication system, thereby avoiding the contamination of the working fluid and reducing the overall system weight and complexity. Gas bearings rely on the relative motion between the rotating shaft and the static bearing components to generate a lubricating film. The amount of load that the bearing can carry therefore depends on fluid properties such as the pressure and viscosity. When applied in turbomachines operating with dense vapors or supercritical flows, compressibility and nonideal thermodynamic effects can largely affect the bearing performance.

A dense vapor is a fluid in thermodynamic states near the saturated vapor line or near the critical point, whereby the compressibility number $Z < 1$ [10]. Such states are characterized by nonideal thermodynamic effects in which molecular interactions are non-negligible. Giuffré et al. [11] recently demonstrated the design optimization of a twin-stage high-speed compressor for an electrically driven vapor compression cycle. The effects of working fluid and nonideal thermodynamic effects were taken into account in the design procedure by the isentropic pressure–volume exponent. Furthermore, Giuffré and Pini [12] presented design guidelines for axial turbines operating with nonideal compressible flows. Molecularly complex fluids with low speed of sound lead to supersonic flows in the nozzles of such turbines, which strongly affects fluid

Turbo Expo, June 24–28, 2024. GT2024.
[1]Corresponding author.
Manuscript received September 16, 2024; final manuscript received October 2, 2024; published online December 11, 2024. Editor: Jerzy T. Sawicki.

dynamic losses. Tosto et al. [13] took a fundamental approach to study how loss mechanisms in internal flows are influenced by both the fluid molecular complexity and the nonideal thermodynamic effects.

Most of the available scientific literature on gas foil bearings considers cases in which air at sea-level conditions is utilized as lubricant. NASA performed an extensive experimental campaign [9] to show the feasibility of supporting high-speed rotors using gas foil bearings lubricated with air. Measured data were used to derive approximate relations for bearing load capacity [14] as well as linearized rotordynamic coefficients [15]. Heshmat et al. [16] presented a modeling technique for bump-type gas foil journal bearings in which the compliant bump strip layer was modeled as an elastic structure. Recent works investigated the performance of hydrodynamic bearings lubricated with dense vapors. Bruckner [17] experimentally investigated the windage losses in gas foil bearings operating at high pressure. Losses associated with inertia effects were shown to increase significantly at elevated pressures. Conboy [18] numerically investigated the performance of gas foil thrust bearings applied in a S-CO_2 closed-Brayton cycle laboratory setup of Sandia National Laboratories. The developed numerical model was coupled to a thermodynamic software program [19] to compute the thermophysical fluid properties. Kim [20] presented a high-level three-dimensional thermohydrodynamic model of a radial foil bearing including turbulence and nonideal thermodynamic effects. In spite of the increasing body of literature, there have been only a few fundamental studies aimed at elucidating the significance of nonideal thermodynamic effects and molecular complexity on the physical behavior of thin film flows in gas bearings.

Guenat and Schiffmann [21] investigated the impact of nonideal thermodynamic effects on gas bearing performance. In their work, a numerical study was performed indicating how the nondimensional load capacity and bearing stability are affected by the thermodynamic state of the fluid. The nondimensional bulk modulus was identified as the main thermophysical parameter affecting the density distribution in the gas film. Results were presented for gas bearings lubricated with various refrigerant fluids. However, the relation between the nondimensional bulk modulus and the nonideal thermodynamic effects was not explicitly addressed. Furthermore, the influence of the fluid molecular structure on bearing performance is not yet fully understood. These aspects are investigated in this work. A physical interpretation of the nondimensional bulk modulus in the context of flows in a nonideal thermodynamic state is presented. Furthermore, the influence of molecular complexity on the nondimensional bearing load capacity and rotor-dynamic characteristics is elucidated using an analysis based on scaling principles and a cubic equation of state.

The article is structured as follows. Section 2 presents the compressible Reynolds equation which is solved numerically using a finite difference method. The perturbation method used to obtain the linearized rotor-dynamic stiffness and damping coefficients is also presented. The outlined methods are used to calculate results for both rigid bearings and gas foil bearings. In Sec. 3, the influence of nonideal thermodynamic effects and molecular complexity on bearing performance is discussed. Finally, the main conclusions drawn from this study are outlined in Sec. 4.

2 Methodology

Both rigid journal bearings and gas foil journal bearings are modeled. The compressible Reynolds equation governing the density distribution within the thin film is presented. A simple elastic model is utilized to account for the bump foil deflections in gas foil bearings. The nondimensional load capacity and critical mass are introduced as the bearing performance parameters used to analyze the influence of nonideal thermodynamic effects and molecular complexity.

2.1 Flow Modeling. The thin film flow separating the rotating shaft from the top foil is modeled using the Reynolds equation. The Reynolds equation was first derived in 1886 by Osborne Reynolds for incompressible flow from the equations of conservation of mass and momentum [22]. Chien et al. [23] present a derivation of the steady Reynolds equation for two-dimensional compressible flows of high-pressure gasses. The derivation can be extended to include unsteady effects and three-dimensional flows, leading to the compressible Reynolds Eq. (1) as used in this work

$$\frac{\partial}{\partial \bar{x}}\left(\frac{\bar{\rho}\bar{h}^3}{\bar{\mu}}G_x\frac{\partial \bar{p}}{\partial \bar{x}}\right)+\frac{\partial}{\partial \bar{z}}\left(\frac{\bar{\rho}\bar{h}^3}{\bar{\mu}}G_z\frac{\partial \bar{p}}{\partial \bar{z}}\right)=\Lambda\frac{\partial(\bar{\rho}\bar{h})}{\partial \bar{x}}+2\Lambda\frac{\partial \bar{\rho}\bar{h}}{\partial \bar{t}} \quad (1)$$

Some of the nomenclature related to the bearing geometry is shown in Fig. 1. The spatial coordinates in the circumferential and axial directions are normalized by the shaft radius, whereas the film thickness is normalized using the nominal bearing clearance. The nondimensional bearing compressibility number or bearing speed number is written as

$$\Lambda=\frac{6\mu_{\text{ref}}\Omega R^2}{p_{\text{ref}}c_0^2} \quad (2)$$

The bearing compressibility number is defined in terms of the rotor speed, the thermodynamic state of the fluid in the bearing compartment, and the bearing geometry. The Poiseuille-like terms on the left-hand side of Eq. (1) represent the effect of pressure gradients on the flow in the circumferential and axial directions. These diffusive effects tend to attenuate the density gradients and are more pronounced for low compressibility numbers Λ. For increasing compressibility numbers, the first right-hand side term of Eq. (1) becomes relevant. This Couette-like term denotes the effect of viscous stresses dragging the fluid into an aerodynamic wedge, thereby causing regions of increased density (and pressure) near the location of minimum film thickness. In this work, the compressibility number will be used as an independent parameter for analyzing bearing performance.

Traditionally, most literature on gas bearings deals with air-lubricated bearings at low pressure, characterized by laminar thin films and thermodynamic state properties calculated with the ideal gas law. In high-pressure lubrication flows, however, the local Reynolds number can reach levels where instabilities arise in the laminar thin film leading to flow transition and turbulence. Although the physics of transition and turbulence is not well represented by a Reynolds-type equation, it has become common practice to account for turbulence effects by means of empirical correction factors. These turbulence correction factors (G_x and G_z) arise in the Poiseuille flow terms of the Reynolds Eq. (1). Several theoretical approaches have been proposed to derive expressions for the

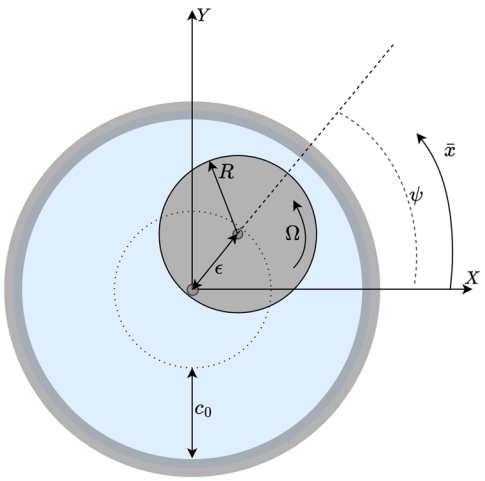

Fig. 1 Schematic figure showing a rigid journal bearing

semi-empirical correction factors [24–26]. In the model of Constantinescu, the semi-empirical correction factors G_x and G_z are written as

$$G_x = \left(1 + \frac{\alpha_x}{12}\mathrm{Re}^{\beta_x}\right)$$
$$G_z = \left(1 + \frac{\alpha_z}{12}\mathrm{Re}^{\beta_z}\right) \tag{3}$$

with the empirical constants $\alpha_x = 0.0136$, $\beta_x = 0.90$, $\alpha_z = 0.0043$, and $\beta_z = 0.96$. It should be noted, however, that the different theories mentioned here all lead to the same qualitative behavior of the turbulence correction factors as a function of the local Reynolds number.

2.2 Thermophysical Property Models. The compressible Reynolds Eq. (1) constitutes a second-order nonlinear partial differential equation for the nondimensional density field defined as $\bar{\rho} = \rho/\rho_{\mathrm{ref}}$. The subscript ref refers to some representative thermodynamic reference state, typically corresponding to the state of the fluid surrounding the bearing. Apart from the density, the thermophysical properties appearing in the Reynolds equation are the normalized dynamic viscosity $\bar{\mu} = \mu/\mu_{\mathrm{ref}}$ and the nondimensional bulk modulus $\bar{\beta} = \beta/p_{\mathrm{ref}}$. The bulk modulus of the fluid is defined as the inverse of the isothermal compressibility and is given as

$$\beta = \rho \frac{\partial p}{\partial \rho}\Big|_T \tag{4}$$

The fluid dynamic performance of turbomachinery components operating with working fluids in nonideal thermodynamic states is often characterized [10] in terms of the specific heat ratio γ and the generalized pressure–volume exponent γ_{Pv}. The latter is used in place of γ to describe isentropic flows in which nonideal thermodynamic effects are of interest such that

$$\left(\frac{p}{\rho}\right)^{\gamma_{\mathrm{Pv}}} = \mathrm{const} \tag{5}$$

Differentiation of the above relation yields [13] the following relation between the isothermal compressibility or nondimensional bulk modulus of the fluid and the parameters γ and γ_{Pv}:

$$\gamma_{\mathrm{Pv}} = \frac{\rho}{p}\frac{\partial p}{\partial \rho}\Big|_s = \gamma \frac{\rho}{p}\frac{\partial p}{\partial \rho}\Big|_T = \frac{\beta\gamma}{p} = \bar{\beta}\gamma \tag{6}$$

The value of the nondimensional bulk modulus is therefore related to the level of nonideality of the fluid state. In thermodynamics, the fluid compressibility factor Z is often used as a measure of the nonideality of a gas. The compressibility factor is defined such that

$$p = Z\rho RT \tag{7}$$

From the definitions of Z, the following relation can be derived between the nondimensional bulk modulus and the compressibility factor:

$$\bar{\beta} = 1 + \frac{\rho_r}{Z}\frac{\partial Z}{\partial \rho_r}\Big|_T \tag{8}$$

From Eq. (8), both the nondimensional bulk modulus and the compressibility factor are one for ideal gasses. The qualitative behavior of both parameters can be explained based on the intermolecular potential. As the pressure of a gas is increased, the distance between molecules decreases, and the intermolecular forces become more significant. In particular, attractive forces between molecules start to dominate. This causes both Z and $\bar{\beta}$ to drop below one. At large pressures, the volume of the molecules becomes non-negligible with respect to the molar volume of the fluid. At low molar volumes, this causes the repulsive forces between molecules to become more significant. When the attractive and repulsive forces are balanced, the compressibility factor Z reaches a minimum and the nondimensional bulk modulus rises above $\bar{\beta} = 1$. Upon further increase of the density, both the bulk modulus and compressibility factor increase. Contours of the nondimensional bulk modulus are plotted on the reduced T–s thermodynamic plane in Fig. 2 for siloxane MM. The plot shows a strong reduction of the nondimensional bulk modulus in the vicinity of the critical point. In the limit of the critical point, the bulk modulus reaches a value of zero. For very high pressures in the supercritical domain, values larger than one are attained. In this region, sometimes considered the "liquid-like" part of the supercritical domain, the fluid behaves increasingly like an incompressible medium. For an ideal gas, the bulk modulus reduces to the pressure and $\bar{\beta}$ is equal to one

$$\bar{\beta}_{\mathrm{ref}} \equiv \frac{\rho_{\mathrm{ref}}}{p_{\mathrm{ref}}}\frac{\partial p}{\partial \rho}\Big|_T = \frac{\rho_{\mathrm{ref}}}{p_{\mathrm{ref}}} RT_{\mathrm{ref}} = 1 \quad \text{for an ideal gas} \tag{9}$$

The nondimensional bulk modulus and dynamic viscosity both depend on the thermodynamic state of the fluid. Traditionally, the thin film flows in gas (foil) bearings have been modeled under the assumption of isothermal flow. The bulk modulus and viscosity are therefore evaluated as a function of the local density and the reference temperature, i.e., $\bar{\beta}(\rho, T_{\mathrm{ref}})$ and $\bar{\mu}(\rho, T_{\mathrm{ref}})$. The nonlinear Reynolds equation is solved iteratively, and the thermophysical properties are updated after each iteration using the density distribution in the film.

For ideal gas lubrication, the dynamic viscosity is typically evaluated using Sutherland's law and only depends on the temperature. Furthermore, for isothermal flow, the nondimensional bulk modulus reduces to the nondimensional density. This allows for a straightforward solution of the Reynolds equation without the necessity of coupling the solver to an external software program for the calculation of thermophysical fluid properties.

In this work, the thermodynamic properties of dense vapors and supercritical fluids are computed using equation-of-state models of varying complexity. The Peng–Robinson cubic equation of state is used to derive theoretical insight. The limited number of parameters involved in the cubic equation of state allows for identifying the most relevant fluid properties relating the molecular complexity to the bearing performance. More complex Helmholtz free energy-based multiparameter equations of state are used to confirm the results. Correlations are used to model the variation of the dynamic viscosity with temperature and density. The implementation of both

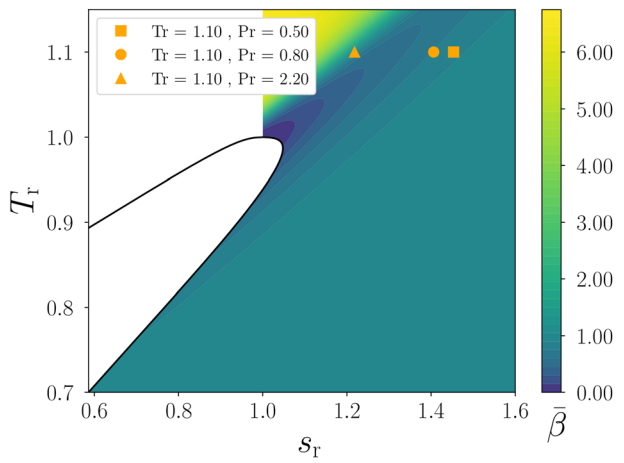

Fig. 2 Considered operating conditions shown on the reduced *T–s* thermodynamic plane of siloxane MM along with contours of the nondimensional bulk modulus $\bar{\beta}$. Plot generated using NICEPROP [27].

the equations of state and the correlations for the dynamic viscosity is done using the COOLPROP [28] and REFPROP [19] software programs.

2.3 Foil Modeling. For gas foil bearings, the increased pressures in the gas film lead to a net force on the top and bump foil structure. The bump foil is a compliant structure that will deform elastically under the action of such forces, resulting in a change in the local film thickness. The foil deflections are accounted for using a simple elastic model. In the model, a linear relation is used between the bump foil deflections w_d and the pressure. The method is well established in literature (e.g., Refs. [16] and [29]) and is not repeated here. It is noted that more accurate models for the bump and top foil deflections exist in literature (e.g., Ref. [30]). The aim of the current work, however, is to investigate the fundamental nonideal thermodynamic effects in the fluid film. For simplicity, the analysis is carried out using this linear elastic model.

Accounting for the structural deflections, the steady-state nondimensional film thickness can be written as

$$\bar{h}_0 = 1 - \epsilon\cos(\bar{x} - \psi) + S\delta\bar{p}_0 \tag{10}$$

where the structural compliance factor [29] is defined as

$$S = \frac{P_{\text{ref}}}{c_0 K_f} \tag{11}$$

2.4 Perturbation Method. The unsteady Reynolds Eq. (1) allows for predicting the time-varying reaction forces exerted by the fluid film on the rotor shaft. The equation can be coupled to the nonlinear rotor-dynamic equations of motion in order to model the evolution of the rotor orbits in time. In this work, however, only the potential onset of bearing instabilities is considered and not the evolution of the unstable rotor motions. Therefore, a perturbation method is applied where a small harmonic motion is introduced around the equilibrium rotor position. The perturbation in the rotor position will introduce a perturbation in the pressure field and the structural deflections of the bump foils, which can eventually lead to instabilities. The perturbed film thickness including the harmonic motions and perturbed foil deflections is written as

$$\bar{h} = \bar{h}_0 - \epsilon_{1X}\cos(\bar{x})e^{i\gamma_{\text{ex}}\bar{t}} - \epsilon_{1Y}\sin(\bar{x})e^{i\gamma_{\text{ex}}\bar{t}} + \frac{S}{(1+i\gamma_S)}(\delta\bar{p}_{1X}\epsilon_{1X} + \delta\bar{p}_{1Y}\epsilon_{1Y})e^{i\gamma_{\text{ex}}\bar{t}} \tag{12}$$

The subscript 0 indicates parameter values at the rotor steady-state equilibrium position, whereas the subscript 1 indicates the perturbations from the steady-state. The rotor motion in X- and Y-directions refers to the inertial axes as shown in Fig. 1. The parameter γ_{ex} is defined as the excitation frequency normalized using the shaft rotational speed Ω. The perturbation in the film thickness will result in a perturbation in the density field as well as the ratio of the bulk modulus to dynamic viscosity appearing in the Reynolds equation

$$\bar{\rho} = \bar{\rho}_0 + \epsilon_{1X}\bar{\rho}_{1X}e^{i\gamma_{\text{ex}}\bar{t}} + \epsilon_{1Y}\bar{\rho}_{1Y}e^{i\gamma_{\text{ex}}\bar{t}} \tag{13}$$

$$\frac{\bar{\beta}}{\bar{\mu}} = \bar{\kappa}_{\text{Te}} = \bar{\kappa}_{\text{Te0}} + \epsilon_{1X}\left(\frac{\partial\bar{\kappa}_{\text{Te}}}{\partial\bar{\rho}}\right)_0\bar{\rho}_{1X}e^{i\gamma_{\text{ex}}\bar{t}} + \epsilon_{1Y}\left(\frac{\partial\bar{\kappa}_{\text{Te}}}{\partial\bar{\rho}}\right)_0\bar{\rho}_{1Y}e^{i\gamma_{\text{ex}}\bar{t}} \tag{14}$$

where the effective bulk modulus $\bar{\kappa}_{\text{Te}}$ is defined following the work of Chien et al. [23] as the ratio of the bulk modulus to dynamic viscosity. It is used here only as a short-hand notation. The partial derivative of the effective bulk modulus to density at constant temperature is written using the chain rule

$$\left.\frac{\partial\kappa_{\text{Te}}}{\partial\rho}\right|_T = \frac{\kappa_{\text{Te}}}{\rho} + \frac{\rho}{\mu}\left.\frac{\partial^2 p}{\partial\rho^2}\right|_T - \frac{\kappa_{\text{Te}}}{\mu}\left.\frac{\partial\mu}{\partial\rho}\right|_T \tag{15}$$

Finally, the turbulence correction factors are a function of the local Reynolds number and therefore of the density, film thickness, and viscosity. The perturbed turbulence correction factors can be obtained in a similar way by application of the chain rule.

The perturbed quantities can be substituted into the unsteady Reynolds Eq. (1). The zeroth- and first-order terms can be grouped and separated leading to the zeroth-order or steady-state Reynolds equation (for $\bar{\rho}_0$) and two first-order or perturbed Reynolds equations (for $\bar{\rho}_{1X}$ and $\bar{\rho}_{1Y}$). The equations are presented in the Appendix. The equations are discretized using a finite difference method. The nonlinear steady-state equation is solved iteratively. The thermodynamic properties and bump foil deflections are updated after every iteration. The first-order equations can be solved straightforwardly, once the steady-state solution is obtained. For both the steady-state and the perturbed Reynolds equations, a periodic boundary condition is applied in the circumferential direction. Dirichlet boundary conditions are applied in the axial direction, imposing the ambient (steady-state) density with zero perturbation at the sides of the bearing.

2.5 Bearing Performance Parameters. Once the steady-state and perturbed density fields are obtained, the pressure field is computed as a function of the density field and the reference temperature. The components of the nondimensional load capacity are computed as

$$W_\alpha = -\int_{-L/D}^{L/D}\int_0^{2\pi}\bar{p}H_\alpha d\bar{x}d\bar{z} \tag{16}$$

$$W = \sqrt{W_x^2 + W_y^2} \tag{17}$$

The nondimensional dynamic bearing impedances can be obtained by integration of the nondimensional perturbed pressure field in a similar way

$$k_{\alpha\beta} + \gamma_{\text{ex}}c_{\alpha\beta} = -\int_{-L/D}^{L/D}\int_0^{2\pi}\bar{p}_{1\beta}H_\alpha d\bar{x}d\bar{z} \tag{18}$$

where α and β take the values X or Y and $H_X = \cos(\bar{x})$ and $H_Y = \sin(\bar{x})$.

The bearing impedances consist of the stiffness and damping coefficients, which are used in a linearized rotor-dynamic model. The critical mass is obtained by finding the whirl frequency canceling the equivalent damping as presented, for example, by Guenat and Schiffmann [21]. The procedure is not repeated here. The nondimensional critical mass is finally defined as

$$\bar{m}_{\text{cr}} = \frac{m_{\text{cr}}\Omega^2 c_0}{R^2 p_{\text{ref}}} \tag{19}$$

3 Results

3.1 Effect of Fluid Molecular Complexity. The effects of the fluid molecular complexity on bearing performance are investigated. Table 1 summarizes the compounds considered in the current analysis along with the relevant properties.

The bearing performance of a rigid journal bearing is numerically investigated for the various compounds. For the purpose of the analysis, a laminar flow regime is assumed by setting the turbulence correction factors to a value of one. The nondimensional load capacity and critical mass are plotted as a function of the compressibility number Λ in Fig. 3. The bearing eccentricity ratio is fixed at $\epsilon = 0.4$. Results are obtained using the Peng–Robinson

Table 1 Fluid properties of some selected fluids

Fluid	T_c (K)	P_c (bar)	ρ_c (kg/m^3)	ω	Molar mass (g/mol)
Helium	5.2	2.3	69.6	−0.384	4.00
Hydrogen	33.1	13.0	31.3	−0.219	2.02
Nitrogen	126.2	34.0	313.3	0.037	28.01
Toluene	591.8	41.3	292.0	0.266	92.14
MM	518.7	19.3	268.4	0.418	162.38
MDM	565.4	14.4	268.2	0.524	236.53
MD2M	599.4	11.4	268.4	0.635	310.69

cubic equation of state for a reduced pressure of $P_r = 0.8$ and a reduced temperature of $T_r = 1.0$ and $T_r = 1.1$. At the critical temperature ($T_r = 1.0$), both the nondimensional load capacity and the nondimensional critical mass are identical for all the considered fluids as indicated by the dotted lines. For a reduced temperature other than the critical temperature (e.g., $T_r = 1.1$), the load capacity and critical mass vary significantly between the different compounds. This difference between working fluids is more significant for increased values of the compressibility number Λ.

The effect of molecular complexity on the bearing performance is explained as follows. The law of corresponding states of van der Waals indicates that different fluids at the same reduced pressure and temperature exhibit similar volumetric behavior and have approximately the same compressibility factors. The results in Fig. 3 are generated using the Peng–Robinson equation of state, although the same conclusions can be drawn using the Soave–Redlich–Kwong (SRK) equation. For the case of the Peng–Robinson (and SRK) cubic equation of state, the deviation of the compressibility factor between working fluids is determined solely by the acentric factor of the fluid [31]. The acentric factor is defined in terms of the reduced vapor pressure at a reduced temperature of $T_r = 0.7$ as

$$\omega = -1 - \log_{10}(P_{\text{vp},r})_{T_r=0.7} \tag{20}$$

It should be noted that the results shown in Fig. 3 are not affected by local variations of the dynamic viscosity in the thin film. At the considered reduced pressure level, the dynamic viscosity does not vary significantly with pressure at constant temperature. Referring to the compressible Reynolds Eq. (1), this leaves the nondimensional bulk modulus as the main parameter introducing fluid dependence to the density distribution. To understand how molecular complexity affects bearing performance, the relation between the nondimensional bulk modulus, the compressibility factor Z, and the acentric factor ω should thus be considered.

The behavior of the compressibility factor and the nondimensional bulk modulus is plotted in Fig. 4 as a function of the reduced pressure for the considered compounds. Results are again obtained using the Peng–Robinson equation at a reduced temperature of $T_r = 1.0$ and $T_r = 1.1$. A characteristic of the Peng–Robinson (and SRK) equation of state is that the compressibility factor becomes independent of the fluid at the critical temperature as indicated by the dotted line. At temperatures other than the critical temperature, the compressibility factor varies between working fluids as a function of the acentric factor. Moreover, Eq. (8) directly relates the nondimensional bulk modulus to the compressibility factor and the reduced mass density. This indicates that, within the limits of validity of the considered cubic equations of state, the nondimensional bulk modulus is a function of reduced temperature and pressure and varies between working fluids only as a function of the acentric factor. This observation is in agreement with the plots of $\bar{\beta}$ in Fig. 4.

Equations of state like the van der Waals and Redlich–Kwong model neglect any anisotropic molecular interactions [32]. The acentric factor was used by Soave as an additional parameter supplementing the Redlich–Kwong equation of state to account for the effects of polarity and nonspherical shapes of the molecules [31]. In general, fluids with more complex molecules tend to have larger values of the acentric factor. A measure for the molecular complexity of a fluid [10] is the number of active degrees-of-freedom N, defined as

$$N = \frac{2}{\delta_\infty(T_c)} = \frac{2c_{v_\infty}(T_c)}{R} \tag{21}$$

in which the ideal gas isochoric specific heat is evaluated at the critical temperature. The acentric factor is plotted versus the number of active degrees-of-freedom in Fig. 5 for the considered fluids. Fluids with larger molecular complexity tend to have a higher acentric factor at least for fluids belonging to the same class (e.g., hydrofluorocarbons, hydrocarbons, and siloxanes).

The current discussion suggests that both the nondimensional load capacity and critical mass are affected by the acentric factor and thus the molecular complexity of the fluid. In the limit of an ideal gas, however, the nondimensional bulk modulus reduces to a constant value of $\bar{\beta}_{\text{ref}} = 1$ as shown by Eq. (9). Therefore, the molecular complexity of the fluid only affects the bearing performance of dense vapors or supercritical fluids where nonideal thermodynamic effects are significant. Furthermore, the increased molecular complexity of a fluid seems to reduce the impact of nonideal thermodynamic effects on bearing performance.

To confirm the observations obtained using the Peng–Robinson equation, the analysis is repeated utilizing the more complex Helmholtz-based multiparameter equations of state models available in Ref. [19]. The resulting nondimensional load capacity is

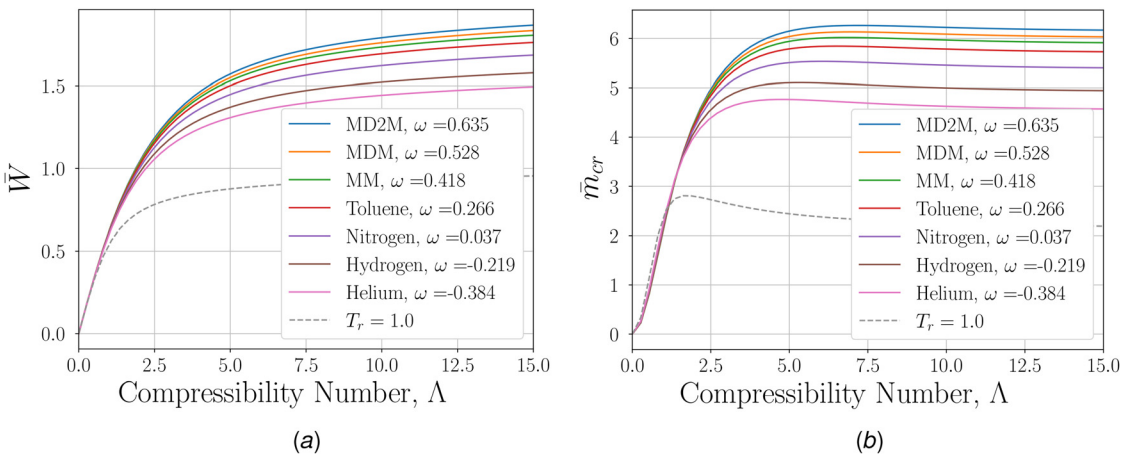

(*a*) (*b*)

Fig. 3 Nondimensional load capacity $\bar{W}$ and critical mass $\bar{m}_{cr}$ at T_r=1.1 for various fluids computed using the Peng–Robinson cubic equation of state. The dotted line represents results for T_r=1.0. (*a*) $\bar{W}$ and (*b*) $\bar{m}_{cr}$.

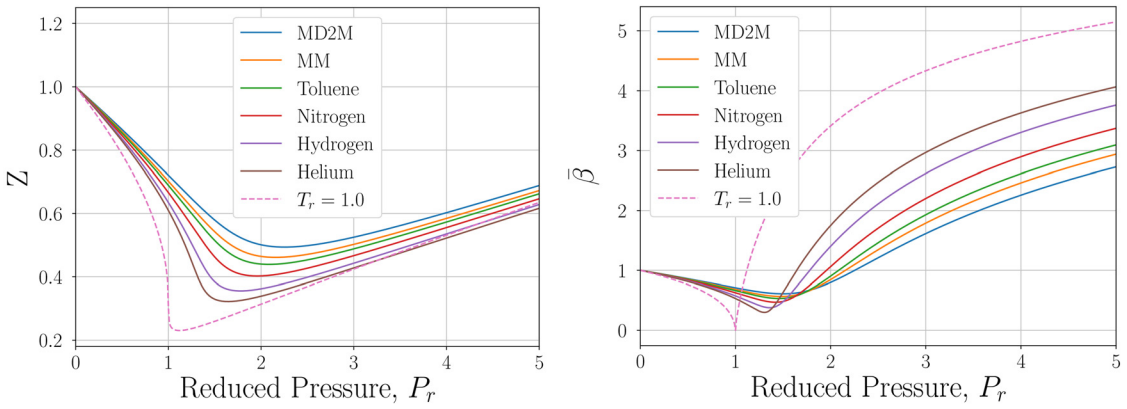

Fig. 4 Compressibility factor *Z* and nondimensional bulk modulus $\bar{\beta}$ at T_r=1.0 for various fluids computed using the Peng–Robinson cubic equation of state. The dotted line represents results for T_r=1.0. (*a*) Compressibility factor, *Z*. (*b*) Nondimensional bulk modulus, $\bar{\beta}$.

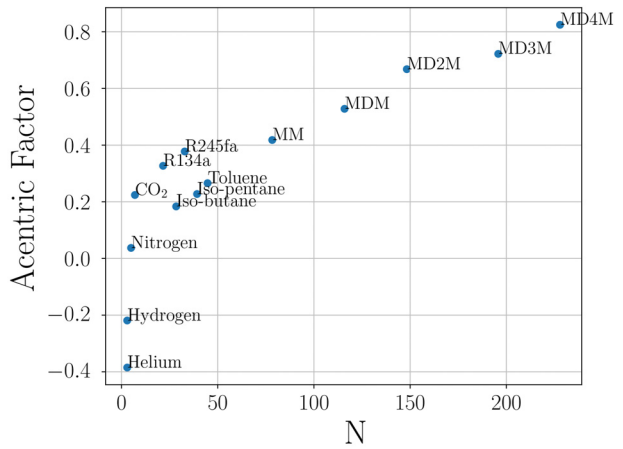

Fig. 5 Acentric factor as a measure of molecular complexity plotted versus the number of active degrees-of-freedom (*N*)

shown in Fig. 6. In general, the results confirm the dependence of the bearing performance on the acentric factor for increased bearing speed numbers. For siloxane MM and MDM, however, similar values are obtained for the nondimensional load capacity even though both compounds have different values of ω. The differences in bearing performance between different lubricant fluids are

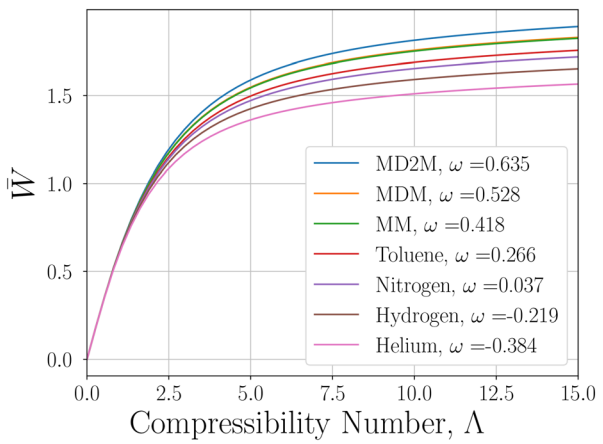

Fig. 6 Nondimensional load capacity $\bar{W}$ at T_r=1.1 for various fluids computed using multiparameter equations of state [19]

therefore not solely related to the acentric factor. However, the results obtained using the multiparameter equations of state seem to confirm the discussed qualitative observations. Similar conclusions can be drawn by plotting the nondimensional critical mass, which has been omitted for brevity.

3.2 Effect of Nonideal Thermodynamic Properties. The numerical model is used to study the influence of nonideal thermodynamic effects on the performance of rigid journal bearings operating with siloxane MM in different thermodynamic states. The considered thermodynamic conditions along with the corresponding nondimensional parameters characterizing the nonideal thermodynamic effects are reported in Table 2. The operating points are also shown on the reduced *T*–*s* thermodynamic plane for siloxane MM in Fig. 2 along with contours of the nondimensional bulk modulus $\bar{\beta}$. The operating points are chosen sufficiently far from the thermodynamic critical point such that the compressible Reynolds Eq. (1) remains valid [23]. The values of the nondimensional load capacity and critical mass obtained at the given thermodynamic conditions are compared to those for MM in ideal gas conditions.

Figure 7(*a*) shows the variation of the nondimensional load capacity with Λ, for the four considered thermodynamic states. At low compressibility numbers, the influence of the thermodynamic state is negligible. As the compressibility number increases, the bearings operating with the working fluid at $P_r = 0.8$ and $P_r = 0.5$ show a lower load capacity compared to the operation with MM in an ideal gas state. This observation is in agreement with the conclusions drawn by Guenat and Schiffmann [21]. Conversely, the nondimensional load capacity significantly increases at the supercritical pressure $P_r = 2.2$.

The influence of the different thermodynamic states is explained using Fig. 8. The figure displays the circumferential distribution of the nondimensional density and pressure at midspan of the bearing for the different operating conditions. An eccentricity ratio

Table 2 Thermodynamic reference states considered for analyzing the influence of nonideal thermodynamic effects on bearing performance

Parameter	Point 1	Point 2	Point 3
T_r	1.1	1.1	1.1
P_r	0.5	0.8	2.2
Z	0.864	0.775	0.423
$\bar{\beta}$	0.857	0.760	1.068
γ	1.050	1.082	1.358
γ_{Pv}	0.900	0.822	1.451

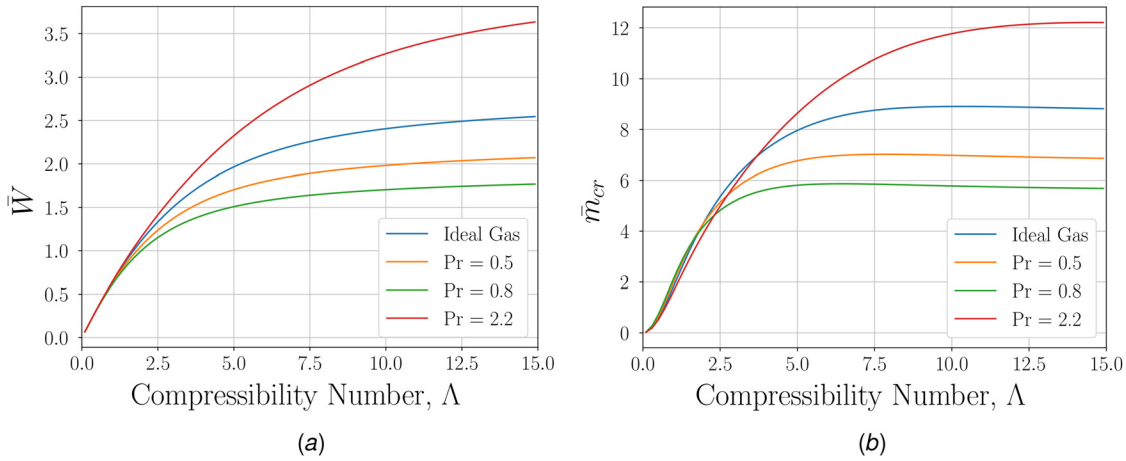

Fig. 7 Nondimensional load capacity $\bar{W}$ and critical mass $\bar{m}_{cr}$ as a function of compressibility number at $\epsilon = 0.4$ for siloxane MM at various thermodynamic conditions: (*a*) $\bar{W}$ and (*b*) $\bar{m}_{cr}$

of $\epsilon = 0.6$ and a compressibility number of $\Lambda = 3.0$ are used to generate the plots. From observation of the compressible Reynolds Eq. (1), it is apparent that a reduced nondimensional bulk modulus decreases the significance of the diffusive terms on the left-hand side of the equation. This is reflected in Fig. 8(*a*), which shows a stronger increase in the nondimensional density for $\bar{\beta} < 1$ as compared to thermodynamic states in which $\bar{\beta} \geq 1$. The corresponding nondimensional pressure distribution is shown in Fig. 8(*b*). In contrast to the density, a stronger increase in the pressure is observed for increasing values of the nondimensional bulk modulus. This in turn leads to increased values of the nondimensional load capacity. For increased values of $\bar{\beta}$, a relatively small increase in density can cause a strong increase in pressure. The bulk modulus can therefore also be interpreted as a measure of the stiffness of the fluid at a particular thermodynamic state. For example, liquids tend to have a relatively large stiffness compared to fluids in nonideal states near the critical point or saturated vapor line.

The nondimensional critical mass is plotted as a function of the compressibility number in Fig. 7(*b*) for the different thermodynamic conditions. Similar trends are observed as compared to those obtained for the nondimensional load capacity. Significant deviations only occur at high values of the compressibility number. In particular, the critical mass is reduced when the working fluid is in nonideal states for which $\gamma_{Pv} < \gamma$ or for which $\bar{\beta} < 1$. The results are in agreement with those presented by Guenat and Schiffmann [21].

3.3 Gas Foil Bearings Stiffness and Damping Coefficients.

The influence of working fluid and nonideal thermodynamic effects on gas foil bearing stiffness and damping coefficients is finally considered. Nondimensional stiffness and damping coefficients are plotted as a function of the nondimensional excitation frequency in Fig. 9. Results are obtained for a gas foil bearing with an axial width-to-diameter ratio of $L/D = 1$ and a bump foil structural compliance ratio of $S = 0.5$. The bearing operates at a compressibility number of $\Lambda = 1.0$ and an equilibrium eccentricity of $\epsilon = 0.8$. Finally, the structural loss factor is set to $\gamma_S = 0$.

Lubrication using hydrogen and siloxane MM is considered as these fluids have significantly different values for the acentric factor. The reference thermodynamic state of both fluids corresponds to a reduced pressure and temperature of $P_r = 0.94$ and $T_r = 1.1$ for which $\bar{\beta} < 1$. Results are compared to a bearing in which the lubricant behaves as an ideal gas. Figure 9 shows an increase in the direct stiffness components (k_{xx} and k_{yy}) with excitation frequency. The cross-coupled stiffness component k_{xy} tends to decrease with excitation frequency. The k_{yx} component increases until the synchronous frequency ($\gamma_{ex} = 1$) and decreases at higher frequencies. Both the direct and cross-coupled damping coefficients shown in Fig. 9 tend to decrease at high excitation frequencies. These observations are in agreement with results presented by San Andrés and Kim [29].

Comparing the different bearing operating conditions, the figures show that both the direct and cross-coupled stiffness and damping

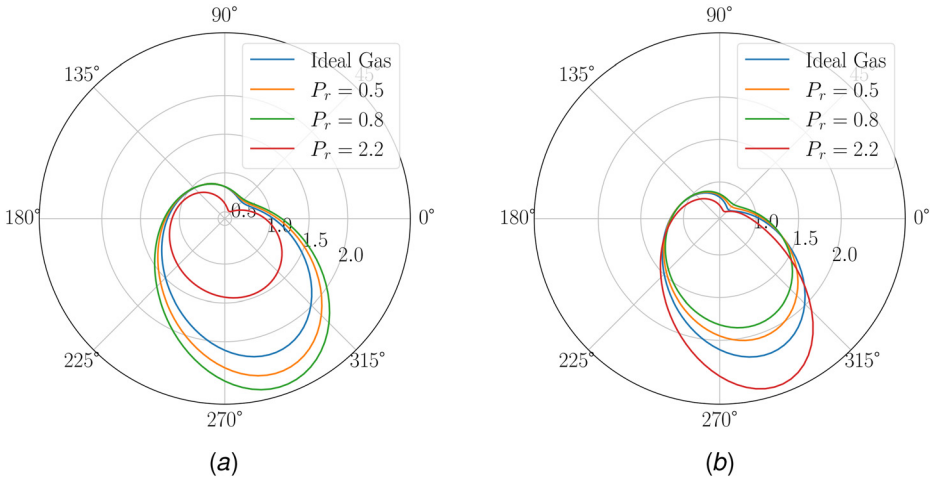

Fig. 8 Polar plots of the nondimensional density and pressure around the circumference of the bearing at midspan. Gray circles indicate isodensity or isopressure lines. (*a*) Nondimensional density and (*b*) nondimensional pressure.

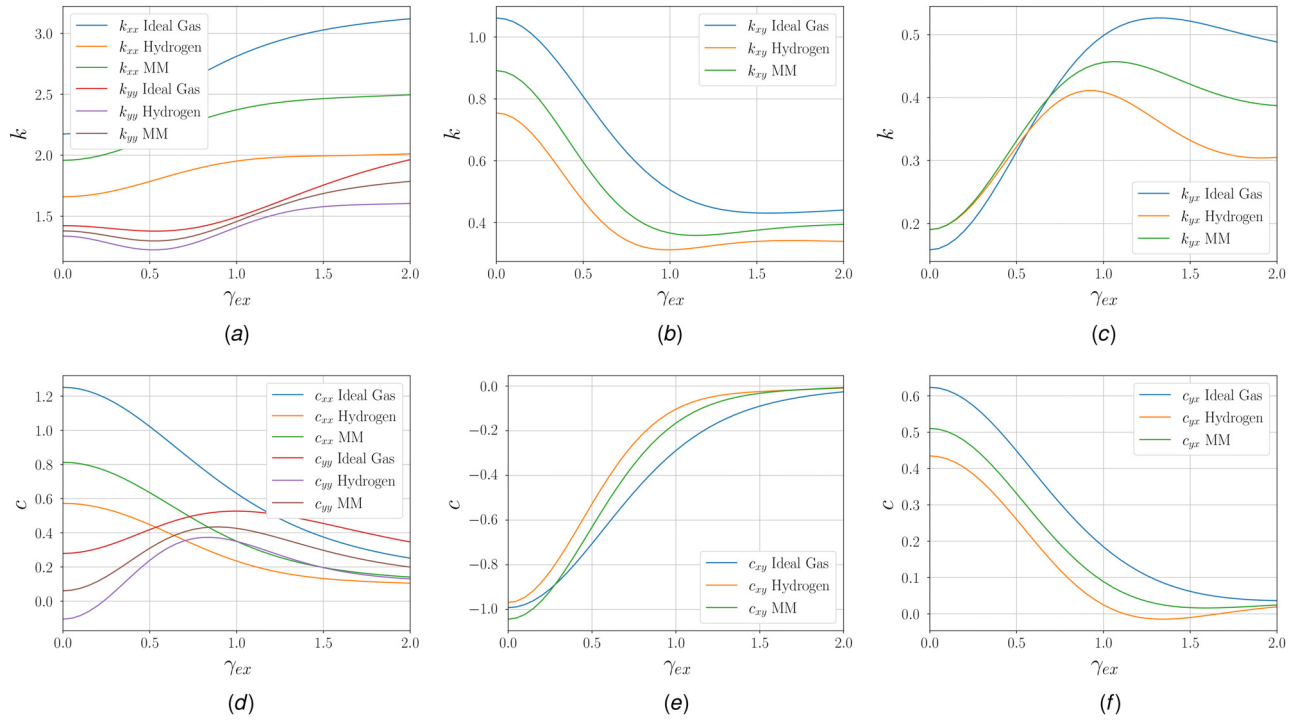

Fig. 9 Nondimensional stiffness and damping coefficients: (*a*) direct stiffness, (*b*) k_{xy}, (*c*) k_{yx}, (*d*) direct damping, (*e*) c_{xy}, and (*f*) c_{yx}

coefficients decrease in magnitude due to the nonideal thermodynamic effects. This corroborates the interpretation of the bulk modulus as a measure of fluid stiffness. Furthermore, referring to Fig. 7(*b*), the net result is a decreased bearing stability as indicated by the reduced critical mass. The effect is more pronounced for hydrogen as compared to MM. This shows the reduced influence of nonideal thermodynamic effects for working fluids made by more complex molecules in correspondence with the discussion in Sec. 3.1.

4 Conclusion

The influence of nonideal thermodynamic effects and molecular complexity of the working fluid on the performance of gas bearings has been investigated. In particular, the nondimensional load capacity and critical mass of rigid journal bearings and the stiffness and damping coefficients of gas foil bearings have been considered. The analysis was performed using equations of state of varying complexity. The following conclusions can be drawn from this work.

(1) The influence of nonideal thermodynamic effects on gas bearing performance can be understood by analysis of the nondimensional bulk modulus. The nondimensional bulk modulus is directly related to the reduced density and the compressibility factor. Reduced values of the nondimensional bulk modulus near the thermodynamic critical point or saturated vapor line decrease bearing performance.
(2) The main parameter characterizing the influence of molecular complexity on gas bearing performance is shown to be the acentric factor. For complex fluids with large acentric factors, the impact of nonideal thermodynamic effects on nondimensional bearing load capacity and rotor-dynamic characteristics is less pronounced.

Acknowledgment

This research is conducted within the research and innovation program Luchtvaart in Transitie, which is co-funded by the Netherlands National Growth Fund.

Funding Data

- Netherlands National Growth Fund.

Data Availability Statement

The datasets generated and supporting the findings of this article are obtainable from the corresponding author upon reasonable request.

Nomenclature

Roman Letters

c = nondimensional damping coefficient
c_0 = nominal bearing clearance (m)
$G_{x,z}$ = turbulence correction factors
h = film thickness (m)
k = nondimensional stiffness coefficient
L = bearing width (m)
m = rotor mass (kg)
p = pressure (Pa)
R = bearing radius (m)
S = structural compliance ratio
T = temperature (K)
W = load capacity (N)
w_d = bump foil deflection (m)
x = circumferential spatial coordinate (m)
X = coordinate in the inertial frame (m)
Y = coordinate in the inertial frame (m)
z = axial spatial coordinate (m)
Z = thermodynamic compressibility factor

Greek Symbols

β = bulk modulus (Pa)
γ = specific heat ratio
γ_{ex} = ratio of excitation frequency to rotor speed
γ_{Pv} = generalized isentropic pressure–volume exponent
γ_S = structural loss factor

ϵ = eccentricity ratio
Λ = bearing compressibility number
μ = dynamic viscosity (kg m^{-1} s^{-1})
ρ = fluid density (kg m^{-3})
ψ = attitude angle (rad)
Ω = rotor speed (rad/s)

Superscripts and Subscripts

r = reduced thermodynamic property
ref = reference value
0 = steady-state value
$1X$ = perturbed quantity due to shaft motion in X-direction
$1Y$ = perturbed quantity due to shaft motion in Y-direction
$\bar{(\cdot)}$ = nondimensional parameter

Dimensionless Groups

Re = Reynolds number

Appendix: Perturbed Reynolds Equation

The perturbed quantities as presented in Sec. 2 are substituted into the unsteady Reynolds Eq. (1). Zeroth- and first-order terms in the density can be grouped and separated to obtain a set of second-order differential equations. The zeroth-order terms govern the steady-state density field as

$$\frac{\partial}{\partial\bar{x}}\left(\bar{h}_0^3 G_{0x}\bar{\kappa}_{\mathrm{Te}0}\frac{\partial\bar{p}_0}{\partial\bar{x}}\right)+\frac{\partial}{\partial\bar{z}}\left(\bar{h}_0^3 G_{z0}\bar{\kappa}_{\mathrm{Te}0}\frac{\partial\bar{p}_0}{\partial\bar{z}}\right)=\Lambda\frac{\partial\left(\bar{\rho}_0\bar{h}_0\right)}{\partial\bar{x}} \tag{A1}$$

The perturbed Reynolds equation for ρ_{1X} and ρ_{1Y} accounting for the effect of bump foil deflections is written as

$$\begin{aligned}
&\frac{\partial}{\partial\bar{x}}\left(\bar{h}_0^3\bar{\kappa}_{\mathrm{Te}0}G_{x0}\frac{\partial\bar{p}_{1\alpha}}{\partial\bar{x}}\right)+\frac{\partial}{\partial\bar{z}}\left(\bar{h}_0^3\bar{\kappa}_{\mathrm{Te}0}G_{z0}\frac{\partial\bar{p}_{1\alpha}}{\partial\bar{z}}\right)\\
&\quad+\frac{\partial}{\partial\bar{x}}\left(\bar{h}_0^3\left(\frac{\partial\bar{\kappa}_{\mathrm{Te}}}{\partial\bar{\rho}}\right)_0\bar{p}_{1\alpha}G_{x0}\frac{\partial\bar{p}_0}{\partial\bar{x}}\right)+\frac{\partial}{\partial\bar{z}}\left(\bar{h}_0^3\left(\frac{\partial\bar{\kappa}_{\mathrm{Te}}}{\partial\bar{\rho}}\right)_0\bar{p}_{1\alpha}G_{z0}\frac{\partial\bar{p}_0}{\partial\bar{z}}\right)\\
&\quad+\frac{\partial}{\partial\bar{x}}\left(\bar{h}_0^3\bar{\kappa}_{\mathrm{Te}0}\left[\left(\frac{\partial G_x}{\partial\bar{\rho}}\right)_0+\left(\frac{\partial G_x}{\partial\bar{\mu}}\right)_0\left(\frac{\partial\bar{\mu}}{\partial\bar{\rho}}\right)_0\right]\bar{p}_{1\alpha}\frac{\partial\bar{p}_0}{\partial\bar{x}}\right)\\
&\quad+\frac{\partial}{\partial\bar{z}}\left(\bar{h}_0^3\bar{\kappa}_{\mathrm{Te}0}\left[\left(\frac{\partial G_z}{\partial\bar{\rho}}\right)_0+\left(\frac{\partial G_z}{\partial\bar{\mu}}\right)_0\left(\frac{\partial\bar{\mu}}{\partial\bar{\rho}}\right)_0\right]\bar{p}_{1\alpha}\frac{\partial\bar{p}_0}{\partial\bar{z}}\right)\\
&\quad+\frac{\partial}{\partial\bar{x}}\left(3\bar{h}_0^2\frac{S}{(1+i\gamma_S)}\delta\bar{p}_{1\alpha}\bar{\kappa}_{\mathrm{Te}0}G_{x0}\frac{\partial\bar{p}_0}{\partial\bar{x}}\right)\\
&\quad+\frac{\partial}{\partial\bar{z}}\left(3\bar{h}_0^2\frac{S}{(1+i\gamma_S)}\delta\bar{p}_{1\alpha}\bar{\kappa}_{\mathrm{Te}0}G_{z0}\frac{\partial\bar{p}_0}{\partial\bar{z}}\right)\\
&=-\frac{\partial}{\partial\bar{x}}\left(\bar{h}_0^2\bar{\kappa}_{\mathrm{Te}0}\left[3G_{x0}+\left(\frac{\partial G_x}{\partial\bar{h}}\right)_0\right]H_\alpha\frac{\partial\bar{p}_0}{\partial\bar{x}}\right)\\
&\quad-\frac{\partial}{\partial\bar{z}}\left(\bar{h}_0^2\bar{\kappa}_{\mathrm{Te}0}\left[3G_{z0}+\left(\frac{\partial G_z}{\partial\bar{h}}\right)_0\right]H_\alpha\frac{\partial\bar{p}_0}{\partial\bar{z}}\right)\\
&\quad+\Lambda\frac{\partial}{\partial\bar{x}}\left(\bar{\rho}_0H_\alpha+\bar{\rho}_0\frac{S}{(1+i\gamma_S)}\delta\bar{p}_{1\alpha}+\bar{\rho}_{1\alpha}\bar{h}_0\right)\\
&\quad+i2\gamma\Lambda\left(\bar{\rho}_0H_\alpha+\bar{\rho}_0\frac{S}{(1+i\gamma_S)}\delta\bar{p}_{1\alpha}+\bar{\rho}_{1\alpha}\bar{h}_0\right)
\end{aligned} \tag{A2}$$

where $\alpha = X$ and $H_X = \cos(\bar{x})$ for $\bar{\rho}_{1X}$ and $\alpha = Y$ and $H_Y = \sin(\bar{x})$ for $\bar{\rho}_{1Y}$. Finally, $\delta\bar{p}_{1\alpha}$ represents the axially averaged perturbation in the pressure in response to a journal displacement.

References

[1] Colonna, P., Casati, E., Trapp, C., Mathijssen, T., Larjola, J., Turunen-Saaresti, T., and Uusitalo, A., 2015, "Organic Rankine Cycle Power Systems: From the Concept to Current Technology, Applications, and an Outlook to the Future," ASME J. Eng. Gas Turbines Power, **137**(10), p. 100801.
[2] Casey, M., Krähenbühl, D., and Zwyssig, C., 2014, "The Design of Ultra-High-Speed Miniature Centrifugal Compressors," 10th European Conference on Turbomachinery Fluid Dynamics and Thermodynamics, ETC10, Lappeenranta, Finland, Apr. 15–19, pp. 506–519.
[3] Lee, Y., Park, D., Kim, T., and Sim, K., 2012, "Development and Performance Measurement of Oil-Free Turbocharger Supported on Gas Foil Bearings," ASME J. Eng. Gas Turbines Power, **134**(3), p. 032506.
[4] Zagarola, M., and McCormick, J., 2006, "High-Capacity Turbo-Brayton Cryocoolers for Space Applications," Cryogenics, **46**(2–3), pp. 169–175.
[5] Kadyk, T., Schenkendorf, R., Hawner, S., Yildiz, B., and Römer, U., 2019, "Design of Fuel Cell Systems for Aviation: Representative Mission Profiles and Sensitivity Analyses," Front. Energy Res., **7**, p. 35.
[6] Schiffmann, J., and Favrat, D., 2009, "Experimental Investigation of a Direct Driven Radial Compressor for Domestic Heat Pumps," Int. J. Refrig., **32**(8), pp. 1918–1928.
[7] Giuffré, A., Colonna, P., and Pini, M., 2022, "The Effect of Size and Working Fluid on the Multi-Objective Design of High-Speed Centrifugal Compressors," Int. J. Refrig., **143**, pp. 43–56.
[8] Conboy, T., Wright, S., Pasch, J., Fleming, D., Rochau, G., and Fuller, R., 2012, "Performance Characteristics of an Operating Supercritical CO_2 Brayton Cycle," ASME J. Eng. Gas Turbines Power, **134**(11), p. 111703.
[9] DellaCorte, C., Radil, K., Bruckner, R., and Howard, S., 2008, "Design, Fabrication, and Performance of Open Source Generation I and II Compliant Hydrodynamic Gas Foil Bearings," Tribol. Trans., **51**(3), pp. 254–264.
[10] Guardone, A., Colonna, P., Pini, M., and Spinelli, A., 2024, "Nonideal Compressible Fluid Dynamics of Dense Vapors and Supercritical Fluids," Annu. Rev. Fluid Mech., **56**(1), pp. 241–269.
[11] Giuffré, A., Colonna, P., and Pini, M., 2023, "Design Optimization of a High-Speed Twin-Stage Compressor for Next-Gen Aircraft Environmental Control System," ASME J. Eng. Gas Turbines Power, **145**(3), p. 031017.
[12] Giuffré, A., and Pini, M., 2021, "Design Guidelines for Axial Turbines Operating With Non-Ideal Compressible Flows," ASME J. Eng. Gas Turbines Power, **143**(1), p. 011004.
[13] Tosto, F., Lettieri, C., Pini, M., and Colonna, P., 2021, "Dense-Vapor Effects in Compressible Internal Flows," Phys. Fluids, **33**(8), p. 086110.
[14] DellaCorte, C., and Valco, M., 2000, "Load Capacity Estimation of Foil Air Journal Bearings for Oil-Free Turbomachinery Applications," Tribol. Trans., **43**(4), pp. 795–801.
[15] DellaCorte, C., 2011, "Stiffness and Damping Coefficient Estimation of Compliant Surface Gas Bearings for Oil-Free Turbomachinery," Tribol. Trans., **54**(4), pp. 674–684.
[16] Heshmat, H., Walowit, J. A., and Pinkus, O., 1983, "Analysis of Gas-Lubricated Foil Journal Bearings," ASME J. Tribol., **105**(4), pp. 647–655.
[17] Bruckner, R., 2009, "Windage Power Loss in Gas Foil Bearings and the Rotor-Stator Clearance of High Speed Generators Operating in High Pressure Environments," ASME Paper No. GT2009-60118.
[18] Conboy, T. M., 2013, "Real-Gas Effects in Foil Thrust Bearings Operating in the Turbulent Regime," ASME J. Tribol., **135**(3), p. 031703.
[19] Lemmon, E. W., Bell, I. H., Huber, M. L., and McLinden, M. O., 2018, "NIST Standard Reference Database 23: Reference Fluid Thermodynamic and Transport Properties-REFPROP, Version 10.0," National Institute of Standards and Technology, Standard Reference Data Program, Gaithersburg, MD.
[20] Kim, D., 2016, "Design Space of Foil Bearings for Closed-Loop Supercritical CO_2 Power Cycles Based on Three-Dimensional Thermohydrodynamic Analyses," ASME J. Eng. Gas Turbines Power, **138**(3), p. 032504.
[21] Guenat, E., and Schiffmann, J., 2018, "Real-Gas Effects on Aerodynamic Bearings," Tribol. Int., **120**, pp. 358–368.
[22] Reynolds, O., 1886, "IV. On the Theory of Lubrication and Its Application to Mr. Beauchamp Tower's Experiments, Including an Experimental Determination of the Viscosity of Olive Oil," Philos. Trans. R. Soc. A, **177**, pp. 157–234.
[23] Chien, S. Y., Cramer, M. S., and Untaroiu, A., 2017, "Compressible Reynolds Equation for High-Pressure Gases," Phys. Fluids, **29**(11), p. 116101.
[24] Constantinescu, V. N., 1959, "On Turbulent Lubrication," Proc. Inst. Mech. Eng., **173**(1), pp. 881–900.
[25] Ng, C., and Pan, C. H. T., 1965, "A Linearized Turbulent Lubrication Theory," ASME J. Basic Eng., **87**(3), pp. 675–682.
[26] Hirs, G. G., 1973, "A Bulk-Flow Theory for Turbulence in Lubricant Films," ASME J. Lubr. Technol., **95**(2), pp. 137–145.
[27] Giuffré, A., and Pini, M., 2022, "NiceProp: An Interactive Python-Based Educational Tool for Non-Ideal Compressible Fluid Dynamics," SoftwareX, **17**, p. 100897.
[28] Bell, I. H., Wronski, J., Quoilin, S., and Lemort, V., 2014, "Pure and Pseudo-Pure Fluid Thermophysical Property Evaluation and the Open-Source Thermophysical Property Library CoolProp," Ind. Eng. Chem. Res., **53**(6), pp. 2498–2508.
[29] Kim, T. H., and San Andrés, L., 2008, "Heavily Loaded Gas Foil Bearings: A Model Anchored to Test Data," ASME J. Eng. Gas Turbines Power, **130**(1), p. 012504.
[30] San Andrés, L., and Kim, T., 2009, "Analysis of Gas Foil Bearings Integrating FE Top Foil Models," Tribol. Int., **42**(1), pp. 111–120.
[31] Invernizzi, C., 2013, *Closed Power Cycles: Thermodynamic Fundamentals and Applications* (Lecture Notes in Energy), Springer, London, UK.
[32] Guardone, A., and Argrow, B. M., 2005, "Nonclassical Gasdynamic Region of Selected Fluorocarbons," Phys. Fluids, **17**(11), p. 116102.